



Cite this: *RSC Adv.*, 2019, 9, 34342

# Engineering a CsPbBr<sub>3</sub>-based nanocomposite for efficient photocatalytic CO<sub>2</sub> reduction: improved charge separation concomitant with increased activity sites†

Xiao-Xuan Guo,<sup>a</sup> Shang-Feng Tang,<sup>a</sup> Yan-Fei Mu,<sup>a</sup> Li-Yuan Wu,<sup>a</sup> Guang-Xing Dong<sup>a</sup> and Min Zhang \*<sup>ab</sup>

Metal-halide perovskite nanocrystals have emerged as one of the promising photocatalysts in the photocatalysis field owing to their low-cost and excellent optoelectronic properties. However, this type of nanocrystals generally displays low activity in photocatalytic CO<sub>2</sub> reduction owing to the lack of intrinsic catalytic sites and insufficient charge separation. Herein, we functionalized CsPbBr<sub>3</sub> nanocrystals with graphitic carbon nitride, containing titanium-oxide species (TiO-CN) to develop an efficient composite catalyst system for photocatalytic CO<sub>2</sub> reduction using water as the electron source. Compared to its congener with pristine CsPbBr<sub>3</sub>, the introduction of TiO-CN could not only increase the number of active sites, but also led to a swift interfacial charge separation between CsPbBr<sub>3</sub> and TiO-CN due to their favorable energy-offsets and strong chemical bonding behaviors, which endowed this composite system with an obviously enhanced photocatalytic activity in the reduction of CO<sub>2</sub> to CO with water as the sacrificial reductant. Over 3-fold and 6-fold higher activities than those of pristine CsPbBr<sub>3</sub> nanocrystals and TiO-CN nanosheets, respectively, were observed under visible light irradiation. Our study provides an effective strategy for improving the photocatalytic activity of metal-halide perovskite nanocrystals, thus promoting their photocatalytic application in the field of artificial photosynthesis.

Received 9th September 2019

Accepted 7th October 2019

DOI: 10.1039/c9ra07236e

rsc.li/rsc-advances

## Introduction

Sunlight-driven photocatalytic CO<sub>2</sub> conversion into high-value added fuels or chemical feedstocks is generally perceived as a promising solution to simultaneously alleviate both energy crisis and environmental problems and has received intense attention in the field of artificial photosynthesis.<sup>1–5</sup> In recent years, most of the attention on this technology has been focused on the development of cost-effective photocatalyst systems.<sup>6–14</sup> In this regard, semiconductor nanocrystals possess excellent properties, such as finely tunable band gaps, large extinction coefficients and long photogenerated carrier lifetimes, and have been actively pursued as photocatalysts in the field of photocatalysis.<sup>15–18</sup> Most recently, metal-halide perovskite nanocrystals, a type of fascinating semiconductor candidates for sunlight harvesting, have also emerged as a class of promising

photocatalysts<sup>19–31</sup> owing to their high defect tolerance and low-cost as well as the facile processing methods,<sup>32–35</sup> which have been dramatically exploited in optoelectronic devices.<sup>36–39</sup>

In the field of photocatalytic CO<sub>2</sub> reduction, however, almost all the pristine metal-halide perovskite nanocrystal photocatalysts exhibit poor photocatalytic activity owing to the lack of intrinsic catalytic sites and insufficient charge separation.<sup>20,22,24,27,29,31</sup> As a learning from the previous studies on conventional metal chalcogenide semiconductor nanocrystals, loading metal-halide perovskite nanocrystals on some two-dimensional (2D) materials, such as graphene oxide<sup>30</sup> or graphitic carbon nitride<sup>22</sup> (g-C<sub>3</sub>N<sub>4</sub>), is expected to enhance the charge separation efficiency, leading to improved photocatalytic activity in CO<sub>2</sub> reduction. However, the lack of intrinsic catalytic sites in these 2D materials also limits the further improvement in their photocatalytic performance in CO<sub>2</sub> reduction. Indeed, our preliminary experiment showed that the CsPbBr<sub>3</sub>@g-C<sub>3</sub>N<sub>4</sub> composite photocatalyst exhibit a little improvement in photocatalytic activity for CO<sub>2</sub> reduction compared to pristine CsPbBr<sub>3</sub> under the irradiation of visible light. It is known that the polymeric material g-C<sub>3</sub>N<sub>4</sub> is a good support material for single atom<sup>40–47</sup> and metal nanoparticles,<sup>48–50</sup> and enhanced

<sup>a</sup>Institute for New Energy Materials and Low-Carbon Technologies, Tianjin University of Technology, Tianjin, 300384, China. E-mail: zm2016@email.tjut.edu.cn

<sup>b</sup>Tianjin Key Laboratory of Organic Solar Cells and Photochemical Conversion, School of Chemistry and Chemical Engineering, Tianjin University of Technology, Tianjin, 300384, China

† Electronic supplementary information (ESI) available: Additional data and experimental details. See DOI: 10.1039/c9ra07236e



solar fuel production can be achieved along with the introduction of these metal catalytic sites.

On the basis of the above analysis, to simultaneously increase the number of catalytic sites and improve the charge separation efficiency of the CsPbBr<sub>3</sub>-based photocatalyst for CO<sub>2</sub> reduction, herein, we functionalized the CsPbBr<sub>3</sub> nanocrystals with graphitic carbon nitride nanosheets, containing titanium-oxide species (TiO-CN), to develop an efficient composite photocatalytic system (coded as CsPbBr<sub>3</sub>@TiO-CN) for photocatalytic CO<sub>2</sub> reduction. Structural characterization revealed that the CsPbBr<sub>3</sub> nanocrystals were closely anchored on 2D TiO-CN *via* N-Br and O-Br bonding, as discussed below. We further systematically compared its structure, light-harvesting ability, band gap alignment, charge generation and separation, as well as the photocatalytic activity in CO<sub>2</sub> reduction, with those of the reference photocatalysts based on pristine CsPbBr<sub>3</sub> nanocrystals and TiO-CN nanosheets.

## Result and discussion

The 2D nanosheets of TiO-CN were prepared according to the method described in a previous publication,<sup>47</sup> which is based on a simple dicyandiamide blowing method.<sup>51</sup> The pristine CsPbBr<sub>3</sub> nanocrystals were synthesized according to a published procedure using a conventional hot injection approach.<sup>52</sup> The CsPbBr<sub>3</sub>@TiO-CN composite was obtained by simply mixing CsPbBr<sub>3</sub> nanocrystals and TiO-CN nanosheets in hexane solvent. The detailed procedure is described in the ESI.† Briefly, CsPbBr<sub>3</sub> nanocrystals and TiO-CN nanosheets were first added into hexane solvent. After ultrasonication for 15 minutes and successive stirring for 2 hours, the color of the solution changed from yellow-green to colorless (Fig. S1†), implying that the CsPbBr<sub>3</sub> nanocrystals dispersed in hexane were successfully loaded onto the TiO-CN nanosheets. Then, the CsPbBr<sub>3</sub>@TiO-CN composite was obtained after centrifugation, followed by drying.

The morphology and composition of the CsPbBr<sub>3</sub> nanocrystals on TiO-CN nanosheets were first evaluated by transmission electron microscopy (TEM) and high-resolution transmission electron microscopy (HRTEM) measurements. As shown in Fig. 1a and b, the CsPbBr<sub>3</sub> nanocrystals could be clearly observed on the sheet-like TiO-CN. The average size of the CsPbBr<sub>3</sub> nanocrystals on TiO-CN was approximately 15 nm (Fig. 1b), which is similar to that of the as-prepared CsPbBr<sub>3</sub> nanocrystals (Fig. S2†). The HRTEM image of the CsPbBr<sub>3</sub> nanocrystals on TiO-CN (Fig. 1c) showed a clear lattice spacing of 0.58 nm, corresponding to that of the (100) plane in the monoclinic CsPbBr<sub>3</sub> phase.<sup>53</sup> As further demonstrated in Fig. 1d, the X-ray diffraction (XRD) pattern of the CsPbBr<sub>3</sub> nanocrystals displayed typical diffraction peaks for monoclinic CsPbBr<sub>3</sub>, which could be well fitted to the standard pattern of JCPDS 00-018-0364. In addition, the XRD pattern of TiO-CN (Fig. 1d) was similar to that of g-C<sub>3</sub>N<sub>4</sub>, which is consistent with a previous result.<sup>47</sup> Moreover, the diffraction peaks of both CsPbBr<sub>3</sub> nanocrystals and TiO-CN nanosheets could be clearly observed in the XRD pattern of the CsPbBr<sub>3</sub>@TiO-CN composite (Fig. 1d). Furthermore, the TEM image (Fig. S3a†) and element

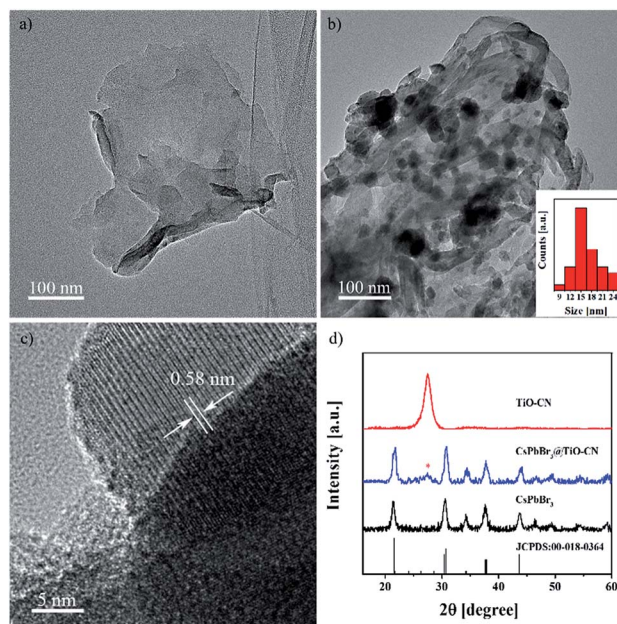


Fig. 1 TEM images of TiO-CN (a) without and (b) with CsPbBr<sub>3</sub> nanocrystal loading. The black dots in panel b are the CsPbBr<sub>3</sub> nanocrystals, and the particle size distribution of CsPbBr<sub>3</sub> is given in the inset in panel b. (c) HRTEM image with the lattice spacing of monoclinic CsPbBr<sub>3</sub> on TiO-CN. (d) XRD patterns of TiO-CN, CsPbBr<sub>3</sub> and CsPbBr<sub>3</sub>@TiO-CN.

mappings (Fig. S3b–h†) of the CsPbBr<sub>3</sub>@TiO-CN composite exhibited a uniform dispersion of cesium, lead and bromine, which indicates that the CsPbBr<sub>3</sub> nanocrystals were homogeneously loaded on the TiO-CN nanosheets.

It is widely recognized that the connection pattern between the components in a composite has an important effect on the photogenerated carrier transfer properties of the composite. Therefore, the interaction behavior of the CsPbBr<sub>3</sub> nanocrystals and the TiO-CN nanosheets was first investigated with the aid of Fourier transform infrared (FTIR) spectrum measurements. In contrast to pristine TiO-CN with a strong characteristic absorption band at ~1241 cm<sup>-1</sup> (Fig. S4†)<sup>54</sup> corresponding to the typical stretching of C–N and C=N groups in TiO-CN, the characteristic absorption band in CsPbBr<sub>3</sub>@TiO-CN displayed an obviously reduced intensity, as presented in Fig. S4.† This phenomenon indicated the existence of a strong bonding interaction between NH<sub>x</sub> and Br<sup>-</sup> correspondingly in TiO-CN and CsPbBr<sub>3</sub>, originating from the easily formed ionic bonding.

The detailed chemical bonding behavior between CsPbBr<sub>3</sub> and TiO-CN was further analyzed by performing high-resolution X-ray photoelectron spectroscopy (XPS) measurements. The N 1s spectrum of TiO-CN could be resolved into four peaks, as presented in Fig. 2a. Apart from the three typical peaks at 398.6, 399.5 and 401.2 eV for nitrogen in different chemical environments (C–N=C, N–(C)<sub>3</sub>, and NH<sub>x</sub>), there was a characteristic peak at 404.5 eV in TiO-CN, which was attributed to the existence of C–N–H in the heterocycles, possessing positive charge localization.<sup>55,56</sup> It is worthwhile to note that this characteristic peak at around 404.5 eV disappeared after loading CsPbBr<sub>3</sub> on



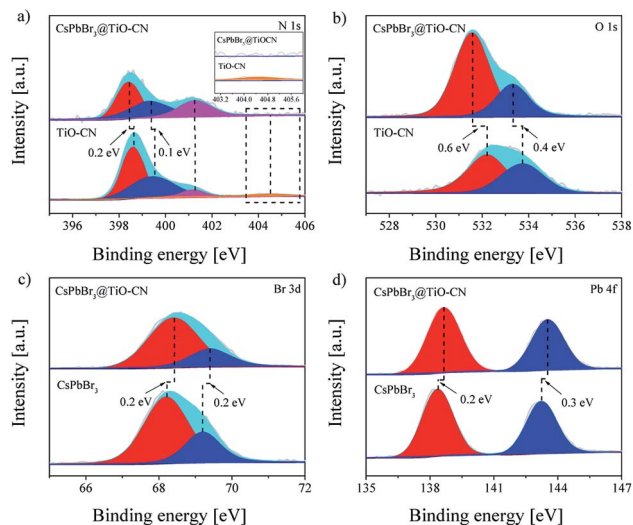


Fig. 2 High-resolution XPS spectra of CsPbBr<sub>3</sub>, TiO-CN and CsPbBr<sub>3</sub>@TiO-CN: (a) N 1s, (b) O 1s, (c) Br 3d and (d) Pb 4f.

TiO-CN, indicating that the localization of the positive charge can be neutralized by the lone pair of electrons from Br on the surface of CsPbBr<sub>3</sub> by forming the chemical bond of C–N–Br. As a result, the N 1s peaks in CsPbBr<sub>3</sub>@TiO-CN showed a perceptible shift to the low-energy region with respect to that of pristine TiO-CN, as observed in Fig. 2a. In addition, the XPS signal for oxygen (Fig. 2b) in the TiO-CN component showed that the binding energy of O 1s in CsPbBr<sub>3</sub>@TiO-CN had clearly negative-shifted in comparison, suggesting the occurrence of a bonding interaction between Br on the CsPbBr<sub>3</sub> surface and OH in TiO-CN. Therefore, loading CsPbBr<sub>3</sub> on TiO-CN would result in electron deficient Br on the CsPbBr<sub>3</sub> surface, which was further demonstrated by the XPS signal of Br 3d. As shown in Fig. 2c, the Br 3d<sub>5/2</sub> and Br 3d<sub>3/2</sub> peaks appeared at 68.2 and 69.2 eV in pristine CsPbBr<sub>3</sub> nanocrystals,<sup>57</sup> which positively shifted to 68.4 and 69.4 eV in CsPbBr<sub>3</sub>@TiO-CN, respectively. Subsequently, the binding energies of Pb 4f<sub>7/2</sub> and Pb 4f<sub>5/2</sub> in CsPbBr<sub>3</sub>@TiO-CN also correspondingly shifted to high energies from 138.4 and 143.2 eV to 138.6 and 143.5 eV, as illustrated in Fig. 2d.

For a typical photocatalyst, a good visible light response is the most basic premise to achieve a visible-light-driven catalytic reaction. Thereby, we first evaluated the light-harvesting capacity of the CsPbBr<sub>3</sub>@TiO-CN composite by recording the electronic absorption spectra of CsPbBr<sub>3</sub>@TiO-CN to preliminarily assess its application potential as a photocatalyst for CO<sub>2</sub> reduction under the irradiation of visible light. As depicted in Fig. 3a, loading the CsPbBr<sub>3</sub> nanocrystals on the TiO-CN nanosheets caused an augmented light response at a desirable longer wavelength compared to pristine TiO-CN owing to the good light-harvesting capacity of CsPbBr<sub>3</sub> in the visible region (Fig. 3a). The photoresponse onset wavelength of CsPbBr<sub>3</sub>@TiO-CN was red-shifted from ~460 nm to ~550 nm. Further, the Tauc plots of CsPbBr<sub>3</sub> and TiO-CN are given in Fig. 3b and c. The band gaps of CsPbBr<sub>3</sub> and TiO-CN were obtained from the intercepts of the extrapolation lines and energy axes as 2.30 and 2.75 eV, respectively.

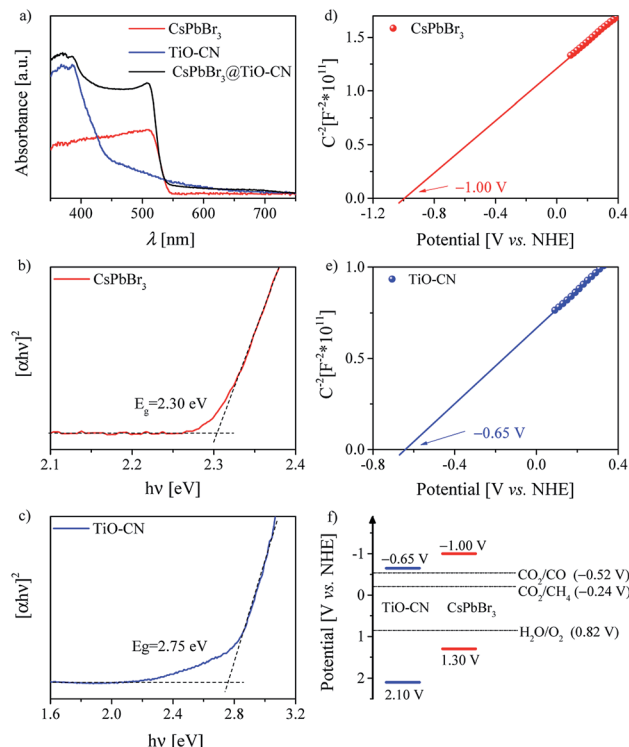


Fig. 3 (a) UV/Vis diffuse reflectance spectra of CsPbBr<sub>3</sub>, TiO-CN and CsPbBr<sub>3</sub>@TiO-CN. Tauc plots of (b) CsPbBr<sub>3</sub> and (c) TiO-CN. Mott–Schottky plots of (d) CsPbBr<sub>3</sub> and (e) TiO-CN. (f) Schematic illustration of the band structures of CsPbBr<sub>3</sub> and TiO-CN derived from the results of flat-band potential and UV/Vis diffuse reflectance spectroscopy measurements.

The energy-offset between the conduction band edges of CsPbBr<sub>3</sub> and TiO-CN plays a pivotal role in determining the dynamic process of photogenerated electron transfer. Since the conduction band edge potential is practically associated with the flat band potential in n-type semiconductors,<sup>58</sup> herein, we employed electrochemical measurements to evaluate the conduction band edge of CsPbBr<sub>3</sub> and TiO-CN by constructing the Mott–Schottky plots, as depicted in Fig. 3d and e. The Mott–Schottky plots of both CsPbBr<sub>3</sub> and TiO-CN clearly exhibited positive slopes, indicating that CsPbBr<sub>3</sub> and TiO-CN were n-type semiconductors. The flat band potentials of CsPbBr<sub>3</sub> and TiO-CN were determined from the corresponding intercepts of the linear plot region with the potential axis to be –1.00 and –0.65 V vs. the normal hydrogen electrode (NHE), respectively, which indicate that the photogenerated electrons in the CsPbBr<sub>3</sub> nanocrystals were transferred to the TiO-CN nanosheets, and the reduction reaction of CO<sub>2</sub> to CO (–0.52 V vs. NHE) by the photogenerated electrons in TiO-CN is thermodynamically permitted. In addition, the corresponding valence band edge potentials of CsPbBr<sub>3</sub> and TiO-CN could be derived from their band gaps and conduction-band edge potentials, as 1.30 and 2.10 V vs. NHE, as illustrated in Fig. 3f, indicating that the photogenerated holes in the TiO-CN nanosheets could be transferred to the CsPbBr<sub>3</sub> nanocrystals, and the photo-generated holes in the CsPbBr<sub>3</sub> nanocrystals had enough





driving force to trigger the water oxidation reaction to generate  $O_2$  (0.82 V vs. NHE).

We speculated that the formation of chemical bonds and favorable energy-offsets between  $CsPbBr_3$  and TiO-CN would facilitate the photogenerated electron transfer from  $CsPbBr_3$  to TiO-CN in the  $CsPbBr_3@TiO-CN$  composite. To check out this, steady state photoluminescence (PL) measurements were firstly recorded to investigate the photoexcited electron transfer processes in the  $CsPbBr_3@TiO-CN$  composite. Herein, pristine  $CsPbBr_3$  was selected as the reference. As depicted in Fig. 4a, the pristine  $CsPbBr_3$  nanocrystals exhibited a strong PL peak at 519 nm, and loading  $CsPbBr_3$  on the TiO-CN surface significantly reduced the PL intensity, indicating the occurrence of a swift photogenerated electron transfer from  $CsPbBr_3$  to TiO-CN. Furthermore, we recorded the time-resolved photoluminescence (TRPL) traces of  $CsPbBr_3$  and  $CsPbBr_3@TiO-CN$  samples to scrutinize the photogenerated electron transfer dynamics using the time-correlated single photon counting technique (TCSPC), as shown in Fig. 4b. An excitation wavelength of 450 nm was picked to selectively excite  $CsPbBr_3$ . The dynamic PL trace of pristine  $CsPbBr_3$  (red symbols) in Fig. 4b can be ascribed to the deactivation of the optically generated excitons in  $CsPbBr_3$  through radiative and nonradiative processes. There was an obviously accelerated PL decay (blue symbols) after loading  $CsPbBr_3$  on the surface of TiO-CN, indicating the opening of a rapid electron transfer channel at the interface between  $CsPbBr_3$  and TiO-CN due to their favourable energy-offset. These traces could be fitted to a multi-exponential function, and the fitting parameters are listed in Table S1.† The value of the amplitude-averaged lifetime of the

pristine  $CsPbBr_3$  nanocrystals was  $\sim 14.8$  ns, which is obviously larger than  $\sim 8.4$  ns for  $CsPbBr_3@TiO-CN$  composites.

The efficient charge separation between  $CsPbBr_3$  and TiO-CN was further elucidated by electrochemical impedance spectroscopy (EIS) and photocurrent response measurements. As depicted in Fig. S5a,† the semicircular arc of the  $CsPbBr_3@TiO-CN$  composite exhibited an obviously smaller diameter in the Nyquist plot compared to those of pristine  $CsPbBr_3$  and TiO-CN, indicating the improvement in the separation efficiency of photogenerated carriers in  $CsPbBr_3@TiO-CN$ . In addition, a remarkably increased photocurrent density could also be detected, as presented in Fig. S5b,† which was over 2 and 3 times higher than those of the pristine  $CsPbBr_3$  and TiO-CN counterparts, respectively, confirming that combining  $CsPbBr_3$  and TiO-CN substantially improved the photogenerated carrier separation efficiency. These phenomena are in line with the results of the abovementioned steady state and transient PL measurements.

Efficient charge transfer and separation between  $CsPbBr_3$  and TiO-CN in the  $CsPbBr_3@TiO-CN$  composite improved the photocatalytic performance, which was demonstrated by the following photocatalytic measurements. The photocatalytic  $CO_2$  reduction reactions were carried out in  $CO_2$ -saturated ethyl acetate/water solution without additional sacrificial reductants under Xe-lamp irradiation with a 400 nm filter at the light intensity of  $100\text{ mW cm}^{-2}$ . Herein, the reaction systems contained a very small amount of water since the metal-halide perovskite is unstable when exposed to a large amount of water.<sup>31</sup> For all the evaluated pristine and composite photocatalyst samples, results from the chromatographic analysis showed that the main product from  $CO_2$  reduction was CO accompanied by a very small amount of  $CH_4$ , and no other reduction products such as  $H_2$  were detected. The product yield of CO was plotted as a function of the photocatalysts, as presented in Fig. 5a. With pristine  $CsPbBr_3$  as the photocatalyst, the yield of CO was only  $38\text{ }\mu\text{mol g}^{-1}$  after 10 h of irradiation, which is similar to the poor photocatalytic activity commonly observed in the recent reports on pristine  $CsPbBr_3$ -based photocatalysts.<sup>20,22,24,27,29,31</sup> On the other hand, pristine TiO-CN also showed very inferior photocatalytic activity with a low CO yield of  $19\text{ }\mu\text{mol g}^{-1}$  from  $CO_2$  reduction under the same irradiation time, as presented in Fig. 5a, which may be ascribed to weak light absorption in the visible region and inferior charge separation.

It should be noted that combining  $CsPbBr_3$  with TiO-CN indeed boosts the photocatalytic activity in  $CO_2$  reduction to CO owing to improved charge separation and an increased number of catalytic sites. As shown in Fig. 5a, the  $CsPbBr_3@TiO-CN$  composite exhibited a significantly improved yield of  $129\text{ }\mu\text{mol g}^{-1}$  for CO formation after 10 h of irradiation, which is over 3 and 6 times higher than those of pristine  $CsPbBr_3$  and TiO-CN, respectively. We also found that the  $CsPbBr_3$  content on the surface TiO-CN plays a pivotal role in the photocatalytic performance of  $CsPbBr_3@TiO-CN$  composite, exhibiting a volcano-type trend, as depicted in Fig. S6.† A lower loading amount of  $CsPbBr_3$  on TiO-CN led to weak light absorption, resulting in a lower yield of CO product for  $CsPbBr_3@TiO-CN$ .

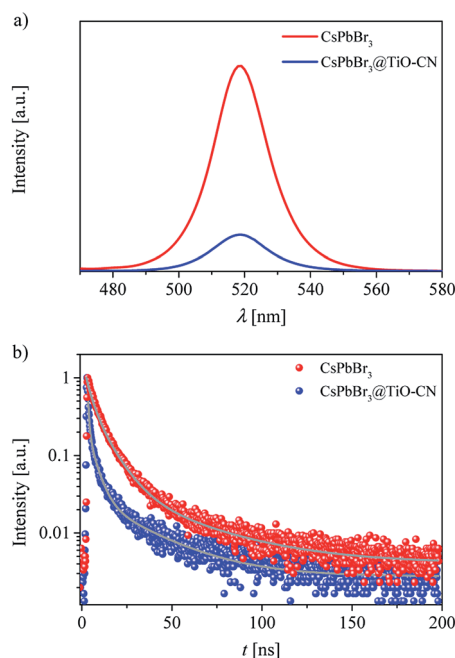


Fig. 4 (a) Photoluminescence spectra of  $CsPbBr_3$  and  $CsPbBr_3@TiO-CN$ . (b) Time-resolved photoluminescence decays of  $CsPbBr_3$  and  $CsPbBr_3@TiO-CN$ . The gray curves are the fitting lines based on a multi-exponential function.



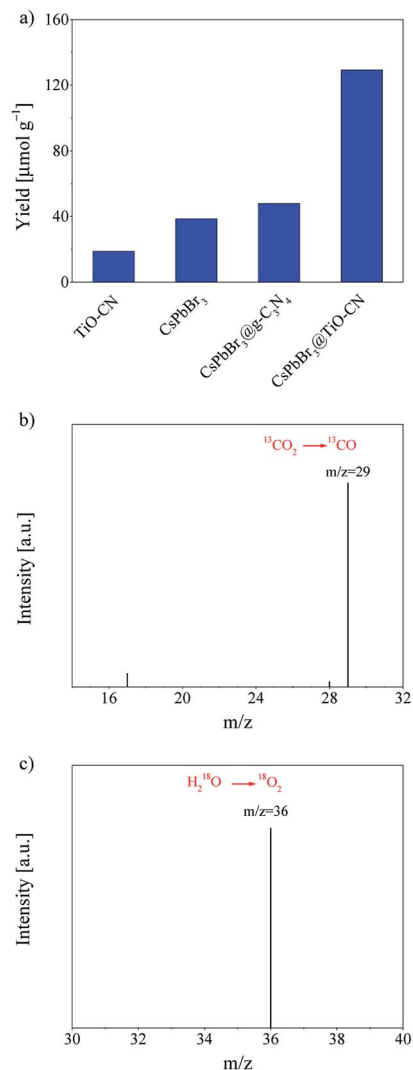


Fig. 5 (a) The yields of CO generated from the photocatalytic  $\text{CO}_2$  reduction reactions with TiO-CN, CsPbBr<sub>3</sub>, CsPbBr<sub>3</sub>@g-C<sub>3</sub>N<sub>4</sub> and CsPbBr<sub>3</sub>@TiO-CN photocatalysts after 10 h of irradiation under a 300 W Xe-lamp with the light intensity of  $100 \text{ mW cm}^{-2}$ . Gas chromatograms and mass spectra (GC-MS) of the solar-driven (b) reduction of  $^{13}\text{CO}_2$  to  $^{13}\text{CO}$  ( $m/z = 29$ ) and (c) oxidation of  $\text{H}_2^{18}\text{O}$  to  $^{18}\text{O}_2$  ( $m/z = 36$ ) using CsPbBr<sub>3</sub>@TiO-CN as the photocatalyst.

The lower yield of CO product for CsPbBr<sub>3</sub>@TiO-CN with a higher loading amount of CsPbBr<sub>3</sub> may be ascribed to the increased amount of CsPbBr<sub>3</sub> without chemical bonding with TiO-CN, resulting in accelerated charge recombination through the surface defect states in CsPbBr<sub>3</sub>. Moreover, to assess the superiority of titanium implantation in g-C<sub>3</sub>N<sub>4</sub>, we prepared a control sample with CsPbBr<sub>3</sub> nanocrystals anchored on 2D g-C<sub>3</sub>N<sub>4</sub> (coded as CsPbBr<sub>3</sub>@g-C<sub>3</sub>N<sub>4</sub>) without titanium implantation. Fig. 5a shows that the yield of CO from  $\text{CO}_2$  reduction in the case of CsPbBr<sub>3</sub>@g-C<sub>3</sub>N<sub>4</sub> was only little higher compared to that of pristine CsPbBr<sub>3</sub> under the same light irradiation condition, which is about 3 times lower than that of the CsPbBr<sub>3</sub>@TiO-CN composite owing to the lack of effective catalytic sites on g-C<sub>3</sub>N<sub>4</sub>, unlike TiO-CN.

The origin of the reduction product CO was further confirmed by a control experiment. In an isotope labelling experiment with  $^{13}\text{CO}_2$  replacing  $^{12}\text{CO}_2$  as the feedstock, gas chromatography/mass spectrometry analysis could clearly identify the major reaction product  $^{13}\text{CO}$  ( $m/z = 29$ ), as shown in Fig. 5b, confirming that the CO was mainly generated from visible-light-driven  $\text{CO}_2$  reduction and not the photo-oxidation of ethyl acetate. On the other hand, the oxidation product  $\text{O}_2$  could also be detected along with CO in the chromatographic analysis results, which is consistent with the common observation in CsPbBr<sub>3</sub>-based photocatalyst systems.<sup>20,27,31</sup> To further verify the origin of the oxidation product  $\text{O}_2$ , an isotope trace experiment with  $\text{H}_2^{18}\text{O}$  was performed in a  $\text{CO}_2$ -saturated ethyl acetate/ $\text{H}_2^{18}\text{O}$  solution with CsPbBr<sub>3</sub>@TiO-CN as the photocatalyst. A major mass signal of  $^{18}\text{O}_2$  with an  $m/z$  value of 36 could be clearly detected, as presented in Fig. 5c, indicating that  $\text{O}_2$  originates from the water oxidation reaction by consuming the photogenerated holes in the CsPbBr<sub>3</sub>@TiO-CN composite, which demonstrates that water is the main electron source for the photocatalytic reduction of  $\text{CO}_2$  to CO.

## Conclusions

In summary, we successfully fabricated a CsPbBr<sub>3</sub>@TiO-CN composite based on a facile process, which can be employed as an efficient photocatalyst for visible-light-driven  $\text{CO}_2$  reduction using water as the electron source. This composite photocatalyst could achieve a significant improvement in CO conversion yield from  $\text{CO}_2$ , which is over 3 and 6 times higher than those of pristine CsPbBr<sub>3</sub> and TiO-CN, respectively. Microstructure characterization revealed that the CsPbBr<sub>3</sub> nanocrystals were closely anchored on 2D TiO-CN *via* N-Br and O-Br bonding. Combining CsPbBr<sub>3</sub> with TiO-CN led to an obviously enhanced of photogenerated carrier separation efficiency, as disclosed by the steady-state and transient photoluminescence data, as well as electrochemical measurements. We also observed the pivotal role of the metal anion in enhancing the photocatalytic activity of the catalyst in  $\text{CO}_2$  reduction, providing a clear clue for further design of metal-halide perovskite-based photocatalysts through material engineering.

## Conflicts of interest

There are no conflicts to declare.

## Acknowledgements

This work was financially supported by Natural Science Foundation of Tianjin City (17JCJC43800), National Key R&D Program of China (2017YFA0700104), NSFC (21790052) and the 111 Project (D17003).

## Notes and references

- 1 X. Li, J. Yu, M. Jaroniec and X. Chen, *Chem. Rev.*, 2019, **119**, 3962–4179.



- 2 J. H. Montoya, L. C. Seitz, P. Chakthranont, A. Vojvodic, T. F. Jaramillo and J. K. Nørskov, *Nat. Mater.*, 2017, **16**, 70–81.
- 3 K. K. Sakimoto, A. B. Wong and P. Yang, *Science*, 2016, **351**, 74–77.
- 4 J. L. White, M. F. Baruch, J. E. Pander III, Y. Hu, I. C. Fortmeyer, J. E. Park, T. Zhang, K. Liao, J. Gu, Y. Yan, T. W. Shaw, E. Abelev and A. B. Bocarsly, *Chem. Rev.*, 2015, **115**, 12888–12935.
- 5 S. Berardi, S. Drouet, L. Francàs, C. Gimbert-Suriñach, M. Guttentag, C. Richmond, T. Stoll and A. Llobet, *Chem. Soc. Rev.*, 2014, **43**, 7501–7519.
- 6 K. C. Christoforidis and P. Fornasiero, *ChemCatChem*, 2019, **11**, 368–382.
- 7 X. Chen and F. Jin, *Front. Energy*, 2019, **13**, 207–220.
- 8 D. C. Grills, M. Z. Ertem, M. McKinnon, K. T. Ngo and J. Rochford, *Coord. Chem. Rev.*, 2018, **374**, 173–217.
- 9 H. Takeda, C. Cometto, O. Ishitani and M. Robert, *ACS Catal.*, 2017, **7**, 70–88.
- 10 C. Li, Y. Xu, W. Tu, G. Chen and R. Xu, *Green Chem.*, 2017, **19**, 882–899.
- 11 H. Abdullah, M. M. R. Khan, H. R. Ong and Z. Yaakob, *J. CO2 Util.*, 2017, **22**, 15–32.
- 12 Z.-F. Huang, J. Song, L. Pan, X. Zhang, L. Wang and J.-J. Zou, *Adv. Mater.*, 2015, **27**, 5309–5327.
- 13 Y. Ma, X. Wang, Y. Jia, X. Chen, H. Han and C. Li, *Chem. Rev.*, 2014, **114**, 9987–10043.
- 14 S. N. Habisreutinger, L. Schmidt-Mende and J. K. Stolarczyk, *Angew. Chem., Int. Ed.*, 2013, **52**, 7372–7408.
- 15 J. Wang, T. Xia, L. Wang, X. Zheng, Z. Qi, C. Gao, J. Zhu, Z. Li, H. Xu and Y. Xiong, *Angew. Chem., Int. Ed.*, 2018, **57**, 16447–16451.
- 16 M. F. Kuehnle, C. D. Sahm, G. Neri, J. R. Lee, K. L. Orchard, A. J. Cowan and E. Reisner, *Chem. Sci.*, 2018, **9**, 2501–2509.
- 17 M. F. Kuehnle, K. L. Orchard, K. E. Dalle and E. Reisner, *J. Am. Chem. Soc.*, 2017, **139**, 7217–7223.
- 18 R. D. Harris, S. B. Homan, M. Kodaimati, C. He, A. B. Nepomnyashchii, N. K. Swenson, S. C. Lian, R. Calzada and E. A. Weiss, *Chem. Rev.*, 2016, **116**, 12865–12919.
- 19 X. Zhu, Y. Lin, J. S. Martin, Y. Sun, D. Zhu and Y. Yan, *Nat. Commun.*, 2019, **10**, 2843.
- 20 L.-Y. Wu, Y.-F. Mu, X.-X. Guo, W. Zhang, Z.-M. Zhang, M. Zhang and T.-B. Lu, *Angew. Chem., Int. Ed.*, 2019, **58**, 9491–9495.
- 21 X. Zhu, Y. Lin, Y. Sun, M. C. Beard and Y. Yan, *J. Am. Chem. Soc.*, 2019, **141**, 733–738.
- 22 M. Ou, W. Tu, S. Yin, W. Xing, S. Wu, H. Wang, S. Wan, Q. Zhong and R. Xu, *Angew. Chem., Int. Ed.*, 2018, **57**, 13570–13574.
- 23 Y.-F. Xu, X.-D. Wang, J.-F. Liao, B.-X. Chen, H.-Y. Chen and D.-B. Kuang, *Adv. Mater. Interfaces*, 2018, **5**, 1801015.
- 24 Y.-F. Xu, M.-Z. Yang, H.-Y. Chen, J.-F. Liao, X.-D. Wang and D.-B. Kuang, *ACS Appl. Energy Mater.*, 2018, **1**, 5083–5089.
- 25 Y. Wu, P. Wang, X. Zhu, Q. Zhang, Z. Wang, Y. Liu, G. Zou, Y. Dai, M.-H. Whangbo and B. Huang, *Adv. Mater.*, 2018, **30**, 1704342.
- 26 H. Huang, H. Yuan, K. P. F. Janssen, G. Solís-Fernández, Y. Wang, C. Y. X. Tan, D. Jonckheere, E. Debroye, J. Long, J. Hendrix, J. Hofkens, J. A. Steele and M. B. J. Roeffaers, *ACS Energy Lett.*, 2018, **3**, 755–759.
- 27 Z.-C. Kong, J.-F. Liao, Y.-J. Dong, Y.-F. Xu, H.-Y. Chen, D.-B. Kuang and C.-Y. Su, *ACS Energy Lett.*, 2018, **3**, 2656–2662.
- 28 S. Park, W. J. Chang, C. W. Lee, S. Park, H.-Y. Ahn and K. T. Nam, *Nat. Energy*, 2016, **2**, 16185.
- 29 Y.-F. Xu, M.-Z. Yang, B.-X. Chen, X.-D. Wang, H.-Y. Chen, D.-B. Kuang and C.-Y. Su, *J. Am. Chem. Soc.*, 2017, **139**, 5660–5663.
- 30 K. Chen, X. Deng, G. Dodekatos and H. Tüysüz, *J. Am. Chem. Soc.*, 2017, **139**, 12267–12273.
- 31 J. Hou, S. Cao, Y. Wu, Z. Gao, F. Liang, Y. Sun, Z. Lin and L. Sun, *Chem.-Eur. J.*, 2017, **23**, 9481–9485.
- 32 Q. A. Akkerman, G. Rainò, M. V. Kovalenko and L. Manna, *Nat. Mater.*, 2018, **17**, 394–405.
- 33 M. V. Kovalenko, L. Protesescu and M. I. Bodnarchuk, *Science*, 2017, **358**, 745–750.
- 34 L. Polavarapu, B. Nickel, J. Feldmann and A. S. Urban, *Adv. Energy Mater.*, 2017, **7**, 1700267.
- 35 X. Li, F. Cao, D. Yu, J. Chen, Z. Sun, Y. Shen, Y. Zhu, L. Wang, Y. Wei, Y. Wu and H. Zeng, *Small*, 2017, **13**, 1603996.
- 36 Q. Zhang and Y. Yin, *ACS Cent. Sci.*, 2018, **4**, 668–679.
- 37 L. N. Quan, F. P. G. de Arquer, R. P. Sabatini and E. H. Sargent, *Adv. Mater.*, 2018, **30**, 1801996.
- 38 M. Ahmadi, T. Wu and B. Hu, *Adv. Mater.*, 2017, **29**, 1605242.
- 39 S. A. Veldhuis, P. P. Boix, N. Yantara, M. Li, T. C. Sum, N. Mathews and S. G. Mhaisalkar, *Adv. Mater.*, 2016, **28**, 6804–6834.
- 40 S. Tian, Z. Wang, W. Gong, W. Chen, Q. Feng, Q. Xu, C. Chen, C. Chen, Q. Peng, L. Gu, H. Zhao, P. Hu, D. Wang and Y. Li, *J. Am. Chem. Soc.*, 2018, **140**, 11161–11164.
- 41 P. Huang, J. Huang, S. A. Pantovich, A. D. Carl, T. G. Fenton, C. A. Caputo, R. L. Grimm, A. I. Frenkel and G. Li, *J. Am. Chem. Soc.*, 2018, **140**, 16042–16047.
- 42 X. Wang, W. Wang, M. Qiao, G. Wu, W. Chen, T. Yuan, Q. Xu, M. Chen, Y. Zhang, X. Wang, J. Wang, J. Ge, X. Hong, Y. Li, Y. Wu and Y. Li, *Sci. Bull.*, 2018, **63**, 1246–1253.
- 43 M. Ou, S. Wan, Q. Zhong, S. Zhang and Y. Wang, *Int. J. Hydrocarbon Eng.*, 2017, **42**, 27043–27054.
- 44 W. Liu, L. Cao, W. Cheng, Y. Cao, X. Liu, W. Zhang, X. Mou, L. Jin, X. Zheng, W. Che, Q. Liu, T. Yao and S. Wei, *Angew. Chem., Int. Ed.*, 2017, **56**, 9312–9317.
- 45 G. Gao, Y. Jiao, E. R. Waclawik and A. Du, *J. Am. Chem. Soc.*, 2016, **138**, 6292–6297.
- 46 X. Li, W. Bi, L. Zhang, S. Tao, W. Chu, Q. Zhang, Y. Luo, C. Wu and Y. Xie, *Adv. Mater.*, 2016, **28**, 2427–2431.
- 47 S. Tang, X. Yin, G. Wang, X. Lu and T. Lu, *Nano Res.*, 2019, **12**, 457–462.
- 48 Y. Zhu, T. Wang, T. Xu, Y. Li and C. Wang, *Appl. Surf. Sci.*, 2019, **464**, 36–42.
- 49 G. Shi, L. Yang, Z. Liu, X. Chen, J. Zhou and Y. Yu, *Appl. Surf. Sci.*, 2018, **427**, 1165–1173.
- 50 H. Li, Y. Gao, Z. Xiong, C. Liao and K. Shih, *Appl. Surf. Sci.*, 2018, **439**, 552–559.



- 51 X. Lu, K. Xu, S. Tao, Z. Shao, X. Peng, W. Bi, P. Chen, H. Ding, W. Chu, C. Wu and Y. Xie, *Chem. Sci.*, 2016, **7**, 1462–1467.
- 52 J. Li, L. Xu, T. Wang, J. Song, J. Chen, J. Xue, Y. Dong, B. Cai, Q. Shan, B. Han and H. Zeng, *Adv. Mater.*, 2017, **29**, 1603885.
- 53 J. Song, J. Li, L. Xu, J. Li, F. Zhang, B. Han, Q. Shan and H. Zeng, *Adv. Mater.*, 2018, **30**, 1800764.
- 54 M. Ou, S. Wan, Q. Zhong, S. Zhang, Y. Song, L. Guo, W. Cai and Y. Xu, *Appl. Catal., B*, 2018, **221**, 97–107.
- 55 J. Fu, B. Zhu, C. Jiang, B. Cheng, W. You and J. Yu, *Small*, 2017, **13**, 1603938.
- 56 P. Yang, H. Ou, Y. Fang and X. Wang, *Angew. Chem., Int. Ed.*, 2017, **56**, 3992–3996.
- 57 J. Liang, C. Wang, Y. Wang, Z. Xu, Z. Lu, Y. Ma, H. Zhu, Y. Hu, C. Xiao, X. Yi, G. Zhu, H. Lv, L. Ma, T. Chen, Z. Tie, Z. Jin and J. Liu, *J. Am. Chem. Soc.*, 2016, **138**, 15829–15832.
- 58 C. Baumanis and D. W. Bahnemann, *J. Phys. Chem. C*, 2008, **112**, 19097–19101.

